Composite patch with negative Poisson's ratio mimicking cardiac mechanical properties: Design, experiment and simulation

Zhicheng Dong [a], Xiaoyang Ren [b], Ben Jia [a], Xuanjia Zhang [c], Xiaopeng Wan [a], Yang Wu [d], Heyuan Huang [b],*

[a] School of Civil Aviation, Northwestern Polytechnical University, Xi'an, Shaanxi, 710072, China
[b] School of Aeronautics, Northwestern Polytechnical University, Xi'an, Shaanxi, 710072, China
[c] Institute of Optics and Electronics, Chinese Academy of Sciences, Chengdu, Sichuan, 610207, China
[d] Department of Cardiovascular Surgery, The First Medical Center of PLA General Hospital, Beijing, 100853, China

ARTICLE INFO

ABSTRACT

Developing patches that effectively merge intrinsic deformation characteristics of cardiac with superior tunable mechanical properties remains a crucial biomedical pursuit. Currently used traditional block-shaped or mesh patches, typically incorporating a positive Poisson's ratio, often fall short of matching the deformation characteristics of cardiac tissue satisfactorily, thus often diminishing their repairing capability. By introducing auxeticity into the cardiac patches, this study is trying to present a beneficial approach to address these shortcomings of the traditional patches. The patches, featuring the auxetic effect, offer unparalleled conformity to the cardiac complex mechanical challenges. Initially, scaffolds demonstrating the auxetic effect were designed by merging chiral rotation and concave angle units, followed by integrating scaffolds with a composite hydrogel through thermally triggering, ensuring excellent biocompatibility closely mirroring heart tissue. Tensile tests revealed that auxetic patches possessed superior elasticity and strain capacity exceeding cardiac tissue's physiological activity. Notably, Model III showed an equivalent modulus ratio and Poisson's ratio closely toward cardiac tissue, underscoring its outstanding mechanical potential as cardiac patches. Cyclic tensile loading tests demonstrated that Model III withstood continuous heartbeats, showcasing outstanding cyclic loading and recovery capabilities. Numerical simulations further elucidated the deformation and failure mechanisms of these patches, leading to an exploration of influence on mechanical properties with alternative design parameters, which enabled the customization of mechanical strength and Poisson's ratio. Therefore, this research presents substantial potential for designing cardiac auxetic patches that can emulate the deformation properties of cardiac tissue and possess adjustable mechanical parameters.

1. Introduction

Ischemic heart disease, leading to conditions such as myocardial infarction (MI) and heart failure caused by cardiac tissue damage, stands as a primary cause of mortality worldwide [1–3]. Presently, approaches to treat cardiac injuries and myocardial necrosis predominantly center around cardiac tissue engineering [4,5]. Within this domain, cardiac scaffolds fabricated from biomaterials have shown significant potential in repairing and regenerating necrotic myocardium, especially when combined with cells or drugs [6,7]. These scaffolds not only help in maintaining and improving myocardial function but also exhibit promising potential in clinical treatments [8–10]. However, a major challenge in developing tissue engineering scaffolds for myocardial repair is the structural and mechanical mismatch with native myocardial tissue [11]. The myocardium, possessing the negative Poisson's ratio property, expands transversely under longitudinal stretching, a feature crucial for enduring the load of daily activities [12–14]. Lacking this characteristic, the transplantation of most traditional scaffolds may potentially lead to loss of cell vitality and function, thereby diminishing the scaffold's efficacy [15]. For instance, some scaffolds designed for cardiac tissue repair have been reported to fail under the mechanical biaxial stress of contracting myocardium, leading to premature death of implanted repair cells [16]. This highlights the deformation mismatch as a key limiting factor in the long-term therapeutic effectiveness of cardiac

scaffolds [17]. Consequently, in designing and optimizing cardiac scaffold structures, researchers must focus not only on mechanical properties but also on ensuring deformation compatibility with surrounding cardiac tissues.

To overcome prevailing challenges in cardiac scaffold design, numerous innovative structures have been developed, including a 4D scaffold approved by Cui et al. [18] and a microneedle scaffold fabricated by Tang et al. [19]. Among these, scaffolds with a negative Poisson's ratio (NPR), also called auxetic structure, stand out due to their mechanical properties closely mirroring those of myocardial tissue, positioning them at the forefront of cardiac scaffold innovation. Such structures uniquely expand vertically when stretched, aligning well with the characteristics of damaged heart tissue, thereby significantly enhancing the durability of the scaffold. The distinct mechanical deformation behavior of NPR meta-structures, which closely matches myocardial tissue relaxation, combined with their superior energy absorption and anti-fracture capabilities, has led to their recognition as promising materials for cardiac scaffolds [20,21]. For instance, Kapnisi et al. employed excimer laser micro-ablation to create a chitosan-polyaniline NPR cardiac scaffold which demonstrated adjustable mechanical strength (ultimate tensile strength ranging from 0.06 ± 0.03 to 1.58 ± 0.9 MPa) and Poisson's ratio (ranging from -1.45 ± 0.2 to -0.15 ± 0.1), catering to various cardiac repair stages [22]. Similarly, Kolken et al. produced auxetic bio-metamaterials with Poisson's ratios from -0.076 to -0.50 by varying size parameters. This material exhibited mechanical properties suitable for human implantation (elastic modulus ranging from 66.3 to 5648 MPa, yield strength ranging from 1.4 to 46.7 MPa) and exceptional fatigue resistance, outperforming many non-auxetic scaffolds of the same material [23]. Furthermore, the effectiveness of biological scaffolds in cell support and delivery is also influenced by their Poisson's ratio. This impact arises because cells interacting with the scaffold respond to its triaxial deformation characteristics, and changes in Poisson's ratio can alter the scaffold's deformation, thus significantly affecting cell division and differentiation [24]. In this context, Yan et al. assessed the influence of 3D scaffolds with NPR properties on pluripotent stem cell (PSC) proliferation and neural cell differentiation. Their findings indicated that auxetic scaffolds notably enhanced PSC differentiation under neural induction conditions [25]. Collectively, these studies affirm that the unique biophysical properties of auxetic materials can enhance structural capability and foster cell differentiation under specific conditions, offering strategies for designing tissue engineering scaffolds to repair myocardial function [26].

However, current cardiac scaffolds are predominantly fabricated from single biological materials, often failing to simultaneously provide the requisite mechanical properties for cardiac function and the biological characteristics necessary to stimulate cardiomyocyte activity and differentiation [27,28]. Consequently, researchers are increasingly pivoting towards cardiac composite patches composed of biomaterial scaffolds and biocompatible polymers [29–31], of which the approach enables the creation of patches that possess both desirable mechanical properties, like elasticity, and biological capabilities, such as cell compatibility [32,33]. Despite the high demand for composite cardiac patches that align with myocardial tissue mechanics and exhibit good biocompatibility, there is a notable dearth of experimental data on the load-bearing mechanical behavior and fatigue performance of auxetic cardiac patches using biocompatible composite materials like hydrogels. Moreover, most scaffolds developed to date feature fixed, unadjustable Poisson's ratios, leading to relatively singular mechanical performance parameters of the resulting patches and limiting their applicability across diverse scenarios [34]. Therefore, designing and fabricating a cardiac patch with adjustable mechanical performance parameters, which meet both the mechanical and biological functional requirements of human myocardium, remains a significant challenge.

Addressing the aforementioned research challenges, this paper seek to tackle the complex issue of myocardial infarction by integrating

auxetic scaffolds with hydrogels known for their excellent biocompatibility. Initially, two auxetic cardiac scaffolds were designed by incorporating chiral rotation and reentrant structures, which were then fabricated using Fused Deposition Modeling (FDM) additive manufacturing technology. Subsequently, the biocompatible PF-AA-AM-Al^{3+} hydrogel was ingeniously integrated with all the designed scaffold types. Mechanical property tests, including tensile and cyclic loading-unloading, were conducted on both auxetic and traditional composite cardiac patches, aiming to determine structural parameters like Poisson's ratio and equivalent modulus, crucial for evaluating their mechanical performance. Further, to examine the deformation and damage behavior of the patches, a cardiac patch model was established in finite element modeling, which combined the elastic-plastic constitutive model of the auxetic scaffold with the viscoelastic constitutive model of the composite hydrogel material. Moreover, the impact of different geometric design parameters on the auxetic structure was also explored, facilitating the control of key performance parameters such as structural Poisson's ratio and modulus ratio. Overall, the two-phase composite auxetic cardiac patches proposed in this work contribute to the structural design of future medical auxetic composite patches and hold great promise as a candidate for curing MI.

2. Materials and methods

2.1. Design of auxetic structure

To align well with the auxetic characteristics required during cardiac repairing and in conjunction with biomimetic design principles [22,35, 36], this study has combined chiral rotation and concave angle structures to devise two types of auxetic scaffolds, being designated as Scaffold II and Scaffold III, as illustrated in Fig. 1a. In Scaffold II, two ribs of the unit cell were arranged in a crosswise manner, with a node deflection angle β of 45°. The additional design parameters were outlined in Table 1. The relative density of all the scaffolds has been calculated. It's worth noting that all cardiac scaffolds of different designs maintain consistent relative densities of approximately '40%', by which comparisons of mechanical properties become more meaningful as the impact of density variations is eliminated. Furthermore, scaffolds with varying relative densities may exhibit differences in structural morphology and interconnectivity, which can significantly influence their effectiveness in promoting inherent negative Poisson's ratio phenomena as well as biological properties such as cell attachment and proliferation. Such variations could potentially lead to unreliable results in our experiments. Moreover, acknowledging that curved geometries can impart higher stretchability and bending flexibility to the structure [37,38], Scaffold III was developed by maintaining the same node-to-node distance L. This model was based on the concept of using curves instead of straight lines to mitigate stress concentration and enhance mechanical properties. In Scaffold III, the arc radii in the x and y directions are defined as $r_x = L/2 \sin\frac{\theta_x}{2}$ and $r_y = L/4 \sin\frac{\theta_y}{2}$.

Simultaneously, a conventional staggered mesh positive Poisson's ratio scaffold, Scaffold I, was designed, drawing upon the research of Lee et al. [39]. For this scaffold, a node deflection angle β of 60° was set to ensure that its nominal area and weight are consistent with the auxetic models designed in this study. It was important to note that the target application for scaffold designs was cardiac injury with a size of 16 mm × 18 mm and a thickness matching that of the heart's epicardium at 0.3 mm, aligning with the dimensions of commonly used cardiac scaffolds in the current medical field [40,41]. All the scaffolds were configured in a 4 × 4-unit cell arrangement, and a rectangular clamp was integrated into the scaffold design to facilitate test loading.
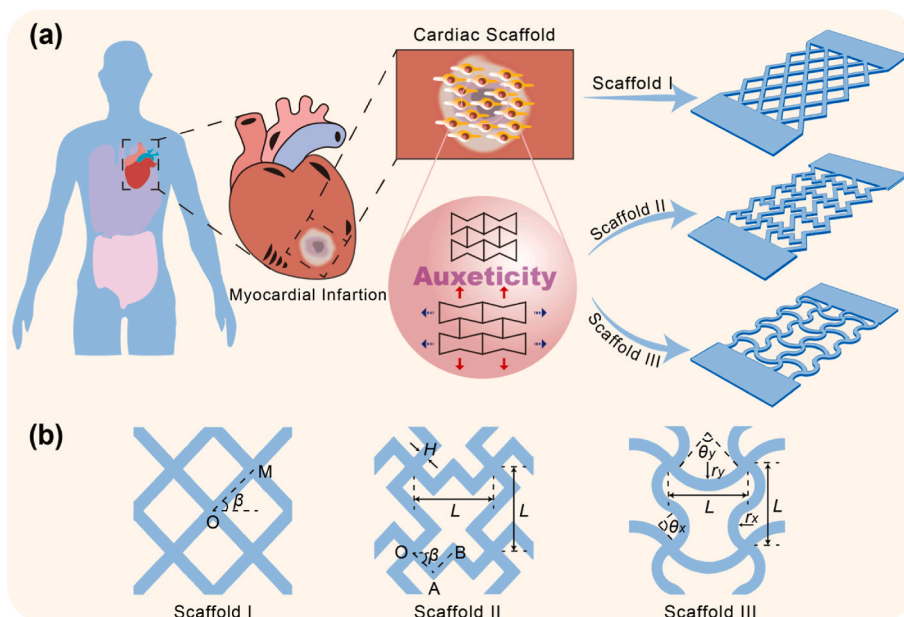
Fig. 1. (a) Designing process of auxetic cardiac scaffolds; (b) Designing parameters of three types of scaffolds.

Table 1
Designing parameters of cardiac scaffolds.

Scaffold I	β		*OM* (mm)		*Relative Density*
	60°		2.94		39.83 %
Scaffold II	*OA* (mm)	*AB* (mm)	*H* (mm)	*L* (mm)	*Relative Density*
	1.52	1.52	0.6	3	40.04 %
Scaffold III	r_x (mm)	r_y (mm)	θ_x	θ_y	*Relative Density*
	0.87	1.90	90°	90°	41.01 %

2.2. Fabrication method

2.2.1. Fabrication of composites materials

In this study, the material used to composite with the scaffold was based on a system that we previously developed. The material was synthesized as a new type of nanocomposite conductive hydrogel through both covalent and non-covalent cross-linking, boasting attributes such as antibacterial conductivity, exceptional toughness, excellent fatigue resistance, and bio-functional compatibility. The specific synthesis process was illustrated in Fig. 2a. The covalent cross-linking involved the free radical polymerization of acryloyl chloride-modified PF127 (PF127-DA), acrylic acid (AA), and acrylamide (AM), aiming to

endow the hydrogel with high stiffness and chemical stability. Additionally, non-covalent cross-linking introduced unique mechanical dissipation mechanisms, such as hydrogen bonding between AM and the strong coordination interaction between AA and Al^{3+}. As a result, the hydrogel exhibited enhanced toughness and fatigue resistance, making it a promising composite material for biological tissue engineering scaffolds [42].

2.2.2. Manufacturing of cardiac scaffolds

In this study, the scaffold material utilized is polycaprolactone (PCL) particle (New Jersey, USA), known for its excellent biocompatibility. As a degradable material, PCL has been previously sanctioned by the U.S. Food and Drug Administration (FDA) for use in biomedical applications and drug delivery devices, making it a prevalent synthetic biodegradable polymer in tissue engineering research [43]. Scaffolds printed using this material exhibit notable design flexibility and long-term stability in application [44]. They also possess the benefits of being non-toxic, harmless, and biocompatible [45,46]. In the specific printing process, fused deposition modeling (FDM) 3D printing technology was employed [47,48]. The nozzle configured in the printing instrument had a minimum diameter of 0.1 mm. After calibration, maintaining a layer height of 0.1 mm not only ensured the accuracy of the printed body but also enhanced printing efficiency, resulting in a scaffold that closely resembled the theoretical model. The extrusion speed during printing was set
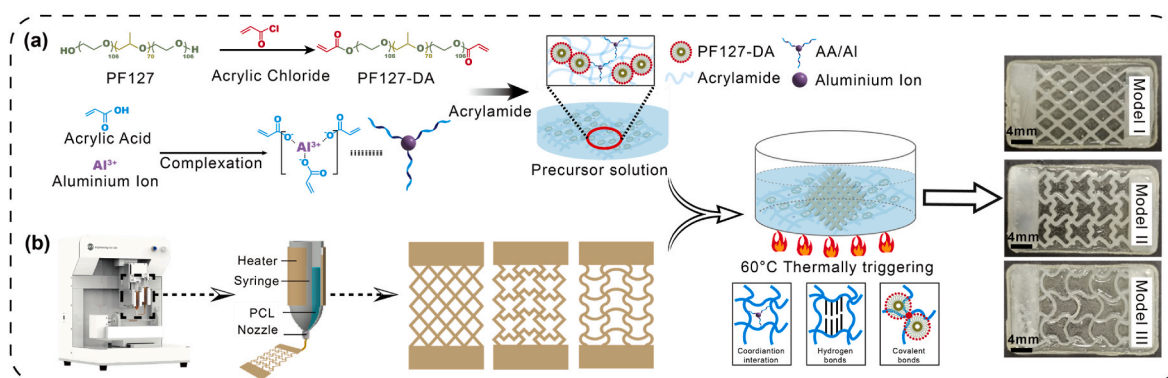

Fig. 2. (a) Preparation of composite hydrogel; (b) 3D printing process of cardiac scaffolds.

at 25 mm/min. Furthermore, the molding quality of the scaffold was influenced by temperature and air pump pressure. Excessively high temperatures could prevent the material from solidifying swiftly, while excessively low temperatures could induce strong internal stress within the material during rapid crystallization, potentially causing local warping of the structure. Similarly, too high air pressure might lead to overly rapid extrusion of the molten material, reducing the porosity of the patch; conversely, too low air pressure may result in a discontinuous structure. After comprehensive consideration, the optimal preparation of the designed scaffold was achieved under an air pressure of 350 kPa and at an environmental temperature of −10°C.

The printing process was depicted in Fig. 2b. PCL particles were placed in the syringe and melted at a low temperature of 90°C for 30 min. Under computer control, the nozzle, equipped with a fine tip of 0.1 mm diameter, and the workbench were respectively moved to designated positions along the x and y axles based on the imported 3D model data. The molten printing material in the syringe was then uniformly extruded onto the −10°C support platform through the nozzle by applying air pressure, allowing for final solidification. After depositing one layer, the nozzle ascended one layer height along the z-axis at a pre-set increment and proceed to deposit the printing material onto the previously solidified layer. This layer-by-layer material accumulation ultimately resulted in the formation of the final PCL scaffold.

2.2.3. Fabrication of composite cardiac patches

Utilizing three types of 3D printed PCL scaffolds as foundations, we infused a high-viscosity conductive composite precursor solution into these scaffolds. This solution was then transformed into a highly cross-linked hydrogel through thermally triggering. The hydrogel exhibited strong adhesion properties, enabling it to seamlessly integrate with the scaffold. Consequently, this method produced a two-phase composite cardiac patch, being designated as Model I, Model II, and Model III, respectively. The composite process was illustrated in Fig. 2. It is essential to highlight that the composite hydrogel we proposed in this study possessed enhanced viscosity to prevent its out-of-plane protrusion during elongation. Moreover, the fabrication method incorporated thermally triggered in-situ polymerization, which significantly improved the bonding capacity within the composite area, thereby minimizing the potential for the separation between these two materials [49].

2.3. Experiments of composites patches

2.3.1. Tensile mechanical tests

The isometric tensile test, as depicted in Fig. 3, comprised two parts: (1) a basic mechanical property test of PCL material; and (2) tensile tests of three composite cardiac patches. The primary objective of the first test was to ascertain the fundamental mechanical property parameters of the PCL printing material, which will serve as input parameters for subsequent numerical simulations. This test was conducted in compliance with ASTM D638 standards, with the specimen fashioned into a dumbbell shape measuring 4 mm × 20 mm × 0.5 mm [50]. An MTS Testwork 4 (USA) universal testing machine was employed for the test, setting the loading speed at 2 mm/min, and the procedure was repeated six times, with five of which have been selected to ensure the accurate acquisition of the necessary material parameters. The test results indicated that the selected PCL printing material possessed an elastic modulus of 446.06 MPa, yield strength of 33.54 MPa, elastic elongation of 7.70%, and a Poisson's ratio of 0.35.

Secondly, uniaxial tensile tests were performed on three types of composite cardiac patches. These tests aimed to acquire the load-displacement curves and identify the failure modes of different structural types under tensile loading. Following these tests, the stress-strain curve for each type was calculated and plotted using the designated formula.

$$\sigma = \frac{F}{A_0} \tag{1}$$

$$\varepsilon = \frac{\Delta L}{L_0} \tag{2}$$

Here, σ represents the tensile nominal stress, A_0 represents the initial cross-sectional area of the specimen, ε represents the tensile nominal strain, ΔL represents the loading displacement, and L_0 represents the initial length of the specimen.

During the testing period, the specifically designed patch was placed on the test bench of an electronic universal testing machine (MTS Testwork 4). The tensile loading speed was set at 2 mm/min, and the experiment was replicated six times for each sample, with five of which have been chosen to ensure reliability. Notably, to prevent evaporation of the water content within hydrogel, a small amount of silicone oil was continually applied to the surface of the sample throughout the test. Upon specimen breakage, the tensile test was concluded, and data
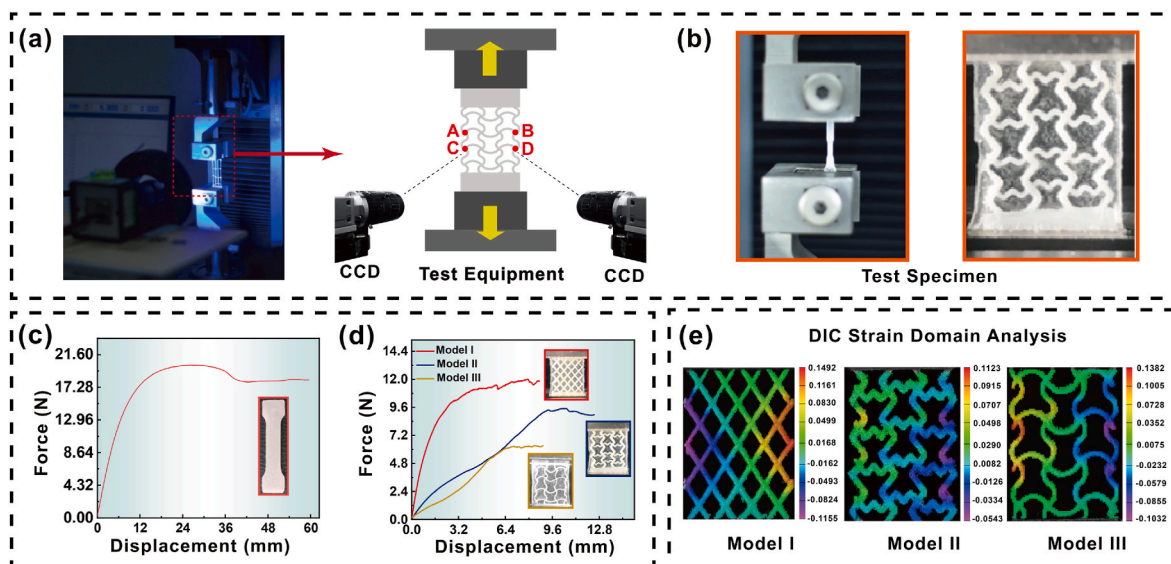

Fig. 3. (a) Diagram of tensile test based on DIC equipment; (b) Specimen of tensile tests; (c) Load-displacement curve of PCL raw material; (d) Load-displacement curve of PCL composite patches; (e) DIC strain domain analysis.

including the load-displacement curve, initial failure load, real-time deformation, and failure mode were recorded. Concurrently, adhering to the standard calculation methods used in mechanical property testing, the stress-strain curve of the specimen under tensile load was derived. The elastic modulus was determined from the slope of the initial section of the stress-strain curve. Table 2 presented a summary of the results obtained from this part of the test, offering a detailed insight into the specific outcomes.

2.3.2. Cyclic loading test

Considering that the heart is constantly exposed to circulatory loads due to expansion and contraction under normal conditions [51], and research indicates that cardiac tissue can endure a maximum strain of 25% during physiological activities, this part aims to assess whether the cardiac composite patch designed herein can adapt to large strains experienced in both typical and extreme situations across different individuals. As for the selection of the formal strain level, the maximum strain endured by cardiac tissue during physical activity is approximately 22%. Additionally, to assess the performance of the patch under higher cyclic strain, we also conducted a fatigue performance test at a 30% stress level. The dual testing conditions allow us to evaluate whether the designed patches meet operational requirements under various states of activity, including extreme strains encountered in extraordinary circumstances. To this end, fatigue performance tests were conducted at two strain levels: 0–22% and 0–30%, respectively. The fatigue life was evaluated through a series of loading-unloading cycles, with the loading-unloading speed set at 10 mm/min. Each test was replicated six times, adhering to ASTM D638 standards. Throughout the test, cyclic load-displacement curves and stress-softening conditions were continuously monitored and recorded.

2.3.3. Measurement of Poisson's ratio based on DIC method

To precisely determine the Poisson's ratio of the structure during the stretching process, this study employed the three-dimensional digital image correlation (DIC) method [52]. The fundamental principle involved integrating digital imaging technology with binocular stereo vision technology. This approach enabled the measurement of three-dimensional coordinates, displacement, and strain on the object's surface during deformation, being achieved by establishing seed points and tracking the speckle pattern present on the surface of the object.

As illustrated in Fig. 3a, two high-speed cameras were utilized to capture key position points on the sample from the onset of stretching until the point of rupture. Here, to minimize the impact of boundary conditions at the upper and lower clamping points, we determined the location for measuring Poisson's ratio to be in the area far away from the loading point, where four points A, B, C, and D were marked on the sample [53–55]. The Poisson's ratio value was then calculated based on the lateral and longitudinal displacements of these position points. The camera settings were adjusted to take photographs at 0.3-s intervals throughout the duration of the tensile test, until the specimen was completely pulled apart. Following this, as demonstrated in the strain analysis field in Fig. 3e, the lateral and longitudinal displacements of the reference points were converted using specific formulas to determine the corresponding lateral and longitudinal strains.

Table 2
Yield strength results of tensile test for composite patches.

	Yield strength (MPa)	Average strength (MPa)	Standard deviation	Discrete coefficient
Model I	0.23, 0.22, 0.21, 0.24, 0.22	0.22	0.011	5.00 %
Model II	0.20, 0.18, 0.19, 0.19, 0.19	0.19	0.007	3.68 %
Model III	0.13, 0.13, 0.12, 0.14, 0.12	0.13	0.008	6.15 %

$$\varepsilon_1^x = \frac{\Delta AB}{AB}$$
$$\varepsilon_1^y = \frac{\Delta AC}{AC} \tag{3}$$

$$\varepsilon_2^x = \frac{\Delta CD}{CD}$$
$$\varepsilon_2^y = \frac{\Delta BD}{BD} \tag{4}$$

The Poisson's ratio was calculated under the definition:

$$\nu_1 = -\frac{\varepsilon_1^x}{\varepsilon_1^y} \tag{5}$$

$$\nu_2 = -\frac{\varepsilon_2^x}{\varepsilon_2^y} \tag{6}$$

To mitigate potential experimental measurement errors, the final Poisson's ratio of the structure was determined by taking the average of two separate calculations of the Poisson's ratio. This approach ensured greater accuracy in the results and could be expressed as $\bar{\nu} = \frac{\nu_1 + \nu_2}{2}$.

2.4. In vitro cytocompatibility test of composite hydrogel

2.4.1. C2C12 cell culture and viability on composite hydrogel

Utilizing the C2C12 cell line, we conducted a direct contact test to assess the in vitro cytocompatibility of the composite hydrogel [56]. Initially, the swollen hydrogel was precisely sectioned into disks measuring 5 mm in diameter and 0.5 mm in height, followed by sterilization through immersion in 75% alcohol. The complete growth medium employed was Dulbecco's Modified Eagle Medium (DMEM) (Gibco), supplemented with 10 % fetal bovine serum (Gibco), 1.0×10^5 U/L penicillin (Hyclone), and 100 mg/L streptomycin (Hyclone). Subsequently, C2C12 cells were seeded at a density of 6000 cells per well in a 96-well plate. After a 24-h cultivation period, the composite hydrogel disks, previously equilibrated in the culture medium, were placed in each well. Cell viability with the presence of the hydrogel was evaluated after culturing for 1 and 3 days using the assay and LIVE/DEAD® Viability/Cytotoxicity Kit assay, respectively. For the alamarBlue® assay, 10 µL of the reagent was mixed with 100 µL of culture medium in each well after removal of the hydrogel disks and the existing medium. The wells was then incubated at 37°C for 4 h, after which 100 µL of the medium from each well was transferred to a 96-well black plate (Costar). After that, fluorescence measurements were obtained with a microplate reader (Molecular Devices), using an excitation wavelength of 560 nm and an emission wavelength of 600 nm. Cells seeded on tissue culture plastic (TCP) without the hydrogel disk served as the positive control. Each group underwent four iterations of these tests. Observations of cell adhesion and viability were accomplished using an inverted fluorescence microscope (IX53, Olympus).

The staining results revealed that the majority of cells within the composite hydrogel groups remained viable after contact with hydrogel disks, mirroring the results observed in the TCP control group (Fig. 4a–b). The findings from the alamarBlue® assay were depicted in Fig. 4e. In Comparison with the TCP group, the PF-AA-AM-Al^{3+} composite hydrogel exhibited a cell viability rate of 92.63%, marginally lower than that of the TCP group. Integrating the insights from both the Live/Dead® and alamarBlue® assays, it was evident that the PF-AA-AM-Al^{3+} composite hydrogel utilized in our research exhibits commendable cytocompatibility, rendering it suitable for biomedical applications.

2.4.2. H9c2 cell culture and viability on composite hydrogel

H9c2 rat cardiomyoblasts, obtained from the Shanghai Cell Bank of the Chinese Academy of Sciences, were maintained under specific conditions. To be specific, H9c2 cells were plated in a 24-well plate at a density of 100,000 cells per well. After 12 h of incubation at 37°C in a
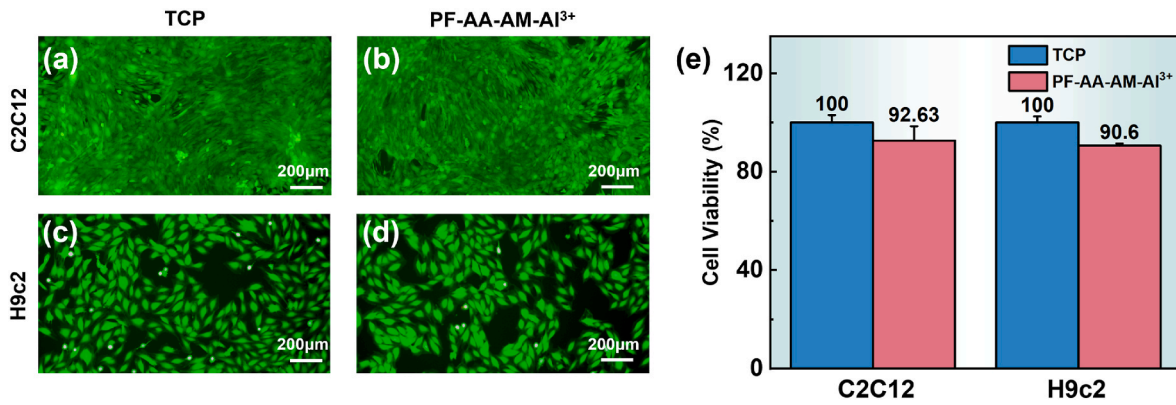
Fig. 4. (a–b) Live/Dead® staining images of C2C12 cells; (c–d) Live/Dead® staining images of H9c2 cells; (e) C2C12 and H9c2 cell viability results.

humidified atmosphere containing 5% CO_2, a disc-shaped composite PF-AA-AM-Al^{3+} hydrogel (5 mm in diameter and 0.5 mm in thickness) was introduced into the culture medium. For the TCP control group, no material was added, and the cells were incubated for 24 h.

The viability of H9c2 cells was then assessed using the AlamarBlue® assay. Initially, the existing medium was removed, and then each well was added 300 μl of growth medium supplemented with 30 μl of AlamarBlue®, followed by an additional 4-h incubation under the same conditions. Subsequently, 100 μl of the culture fluid from each well was transferred to a 96-well black plate (Costar). Fluorescence measurements were performed using a microwell plate reader (Molecular Devices) at an excitation wavelength of 560 nm and an emission wavelength of 600 nm, with six replicates per condition.

H9c2 cells, a rat cardiomyoblast cell line, are extensively utilized for evaluating biomaterials in cardiac therapy. The viability of these cells on the composite hydrogel was assessed after 24 h of cultivation, with the results shown in Fig. 4c–d. In this technique, live cells emit green fluorescence, whereas dead cells exhibit red fluorescence. Predominantly green fluorescence in the images suggested high cell viability. Quantitative analysis in Fig. 4e revealed that H9c2 cell viability reached 90.60 + 0.91%, demonstrating that the composite hydrogel we used possessed non-toxicity and had excellent cytocompatibility with H9c2 cells.

2.5. Statistical analysis

Quantitative measurements were expressed as mean ± standard deviation (SD). Student's t-test was performed. The significant difference was considered when $*p < 0.05$, $**p < 0.01$, $***p < 0.001$.

3. Numerical analysis

3.1. Finite element model

3.1.1. Elastoplastic constitutive model for PCL Scaffold

To elucidate the deformation mechanism and failure mechanism of the auxetic patch in this study, the elastic-plastic model of the PCL scaffold material was first established. During the initial tension stage, the entire structure underwent linear elastic deformation, with the stress state point residing within the yield surface in stress space. In the unidirectional stress state, the stress-strain relationship during this linear elastic phase adhered to Hooke's law, and its constitutive relationship is defined by the generalized Hooke's law. As the stretching simulation progressed, the Mises yield condition, which is particularly apt for polymer materials, was employed to ascertain whether the PCL scaffold transitioned into the plastic phase. At this juncture, the tensile and shear yield limits of the material satisfy the equation $\sigma_Y = \sqrt{3}\tau_Y$. With this relationship established, the Mises yield condition can be expressed in the following standard form:

$$(\sigma_1 - \sigma_2)^2 + (\sigma_2 - \sigma_3)^2 + (\sigma_3 - \sigma_1)^2 = 2\tau_Y^2 \tag{7}$$

After the completion of the plastic phase, the material began to suffer damage, manifested as yield stress and a reduction in elasticity. At this stage, $\bar{\varepsilon}_0^{pl}$ is defined as the plastic strain corresponding to the onset of damage, and $\bar{\varepsilon}_f^{pl}$ is defined as the maximum strain corresponding to the point of complete fracture. Within finite element software, modeling damage involves identifying the starting point of damage and its subsequent evolution. The equivalent plastic strain $\bar{\varepsilon}_D^{pl}$, at which damage initiated, was typically predicted through a phase-only flexibility criterion model, which is generally considered to correlate with stress triaxiality η and strain rate $\dot{\bar{\varepsilon}}_D^{pl}$. Damage onset occurred when the plastic strain reached the threshold defined by the flexibility criterion. The relevant equation at this stage is as follows:

$$\omega_D = \int \frac{\Delta d\bar{\varepsilon}^{pl}}{\bar{\varepsilon}_D^{pl}(\eta, \dot{\bar{\varepsilon}}^{pl})} = 1 \tag{8}$$

3.1.2. Viscoelastic constitutive model for PF-AA-AM-Al^{3+} hydrogel

The composite hydrogel, exhibiting both elastic and viscous characteristics, can be conceptualized as an amalgamation of spring and viscous models, arranged either in series or parallel. At present, the classic viscoelastic models include Maxwell model, Kelvin model, etc. In our study, to represent the hydrogel's viscoelastic nature more precisely, we integrated these two models, resulting in the formulation of a generalized Maxwell model.

The differential constitutive equation for the generalized Maxwell model, derived by applying the Boltzmann superposition principle to the components of a single Maxwell model, is presented as follows:

$$\sigma(t) = \varepsilon_0 E(t) + \int_0^t E(t-s) \frac{d\varepsilon(s)}{ds} ds \tag{9}$$

Here, $\sigma(t)$ represents the stress, ε_0 represents the initial strain value, t represents the current time, and represents the delay time. $E(t)$ is the relaxation modulus, which is derived by integrating and rearranging the equation. The specific equation is as follows:

$$E(t) = E_\infty + \sum_{i=1}^{N} E_i e^{-\frac{t}{\tau_i}} \tag{10}$$

Meanwhile, given that the hydrogel material is isotropic, its elastic relaxation modulus aligns with the shear relaxation modulus. Consequently, to convert the elastic relaxation modulus into a quantifiable shear relaxation modulus for use in finite element analysis software, the following formula is employed:

$$G(t) = \frac{E(t)}{2(1+\mu)} \tag{11}$$

Here, μ refers to Poisson's ratio, and $G(t)$ is the shear relaxation modulus.

By substituting the aforementioned equation and normalizing the result, the following equation can be obtained:

$$g(t) = 1 - \sum_{i=1}^{N} g_i \left(1 - e^{-\frac{t}{\tau_i}} \right) \tag{12}$$

Here, τ_i represents the relaxation time, g_i is the dimensionless material parameter, $g(t)$ represents the normalized shear relaxation modulus, t represents time, and N represents the number of terms in the Prony series. For the model discussed in this article, the hydrogel is assumed as an incompressible and isotropic materials, and the superposition of two Maxwell models is employed, thus $N = 2$. Based on the stress relaxation test results, the Prony series equation for the generalized Maxwell model of the PF-AA-AM-Al^{3+} is formulated as follows:

$$g(t) = 0.343 + 0.151 e^{-t/77.08} + 0.122 e^{-t/785.95} \tag{13}$$

3.2. Establishment and verification of composite patch finite element model

The commercial finite element software 'Abaqus' was employed to simulate the load-bearing and deformation behavior of the auxetic patches under large deformation, which was key to analyzing their load-bearing capacity and failure behavior. Initially, geometric finite element models, mirroring the actual size of the specimen, were developed for three different configurations based on structural design parameters. An elastic-plastic constitutive model was used to describe the deformation behavior of the PCL scaffold layer under load, setting the PCL modulus at 46.06 MPa and Poisson's ratio at 0.35. Additionally, a viscoelastic constitutive model was utilized to predict the mechanical response of the composite hydrogel material in the filling layer under load, using parameters derived from the original study (modulus at 0.25 MPa and Poisson's ratio at 0.37). Prior to finite element analysis, the model was divided using a tetrahedral mesh, and C3D4R element attributes were assigned to the mesh. To mimic the composite patch's loading conditions in practical application, one side of the patch was fully constrained, while the composite hydrogel was affixed to the surface of the PCL scaffold. The other end of the patch was subjected to displacement loading, as depicted in Fig. 5.

Fig. 6a presents a side-by-side comparison of the stress-strain test results and numerical simulations for the three cardiac patches. The figure demonstrates a strong correlation between the numerical simulation outcomes and the experimental data, affirming the accuracy of the elastic-plastic constitutive model of the PCL scaffold and the viscoelastic model of the composite hydrogel established in this study. Initially, the stress-strain curves for all the patches exhibit linear trends during the early loading stages. Upon increased loading, the stress-strain curves of the auxetic patches, which incorporate chiral rotation and concave expansion features, ascend more gradually, displaying a step-like buffering region. This indicates a high level of congruence between the

elastic portion of the numerical model and the experimental curve. Moreover, the figure reveals that the numerical simulation results for the model are marginally lower than the experimental values. This discrepancy could be attributed to variations introduced during the specimen manufacturing process.

Fig. 6b extends the analysis by comparing the modulus ratio from both experimental tests and numerical simulations. During testing, the structures were subjected to simulated loading in the primary x and y directions. In the case of conventional patches, the experimentally determined transverse-to-longitudinal modulus ratio was found to be 7.45% higher than the finite element analysis results. For patches with auxetic structure, the trends observed in both finite element simulations and experimental outcomes were largely consistent. Notably, the transverse modulus in the model was higher than the longitudinal modulus, indicating consistent anisotropy in these structures. The comparative analysis of the modulus ratios reveals minimal significant differences between the test and finite element results across all three structural types, suggesting a strong correlation of the finite element model with the experimental data.

In analyzing the changes in Poisson's ratio during the tensile process, the value for the structure was calculated using the relative displacement of points A, B, C, and D, with the results presented in Fig. 6c. The figure revealed that the Poisson's ratio of Model I remained relatively constant until it reached the point of fracture. Conversely, the auxetic patches, Model II and III, displayed a trend in Poisson's ratio change that aligned with the experimental results. Specifically, as the strain increased, the Poisson's ratio values rose approximately linearly. Notably, during the test phase, the auxetic patches exhibited a slightly faster increase in Poisson's ratio compared to the numerical simulation. This discrepancy was likely due to the limitations of 3D printing technology, which may not guarantee perfect geometric uniformity in each segment of the printed part. Consequently, some transverse ribs of the structure might have buckled or twisted during testing, altering the force transmission path and reducing transverse support. In contrast, the finite element model was less susceptible to these structural issues due to its ability to precisely control the dimensions of each segment and the sophisticated meshing and attribute settings of the software. As a result, the lateral strain of the test specimen decreased more rapidly, and the rate of lateral strain change rate of the test structure exceeded that in the simulation, leading to a higher rate of increase in Poisson's ratio in the test results compared to the finite element analysis outcomes.

Table 3 encapsulated the comparative analysis of three key performance evaluation indicators - yield strength, Poisson's ratio, and modulus ratio - for both the tested and simulated structures. The data revealed that the numerical simulation errors were confined within an 11% margin, demonstrating a substantial consistency between the experimental and finite element results. This congruence underscored the high accuracy of the composite patch model developed in this study. Consequently, this model was adept at predicting the mechanical behavior of the patch under real-world loading conditions.

3.3. Mechanism analysis of auxetic patches

To elucidate the deformation mechanism of the auxetic patches under tension, in this part, we mainly focused on a specific deformation unit within the central area of Model II. By employing the energy method, the unit cell was theoretically analyzed to better understand its stress deformation behavior when being stretched. It is worth noting that while the structure could be conceptualized as consisting of ribs, the shear deformation of these ribs was relatively minor and could be disregarded. Therefore, the analysis primarily considered the axial and bending deformations of the ribs during the structural stress assessment [57].

Considering the symmetry of the structural unit and the applied load, a single deformation unit was constituted of a chiral unit featuring both symmetric and anti-symmetric structures, with each unit encompassed 8
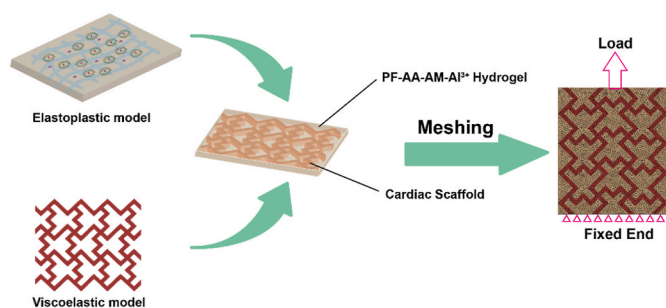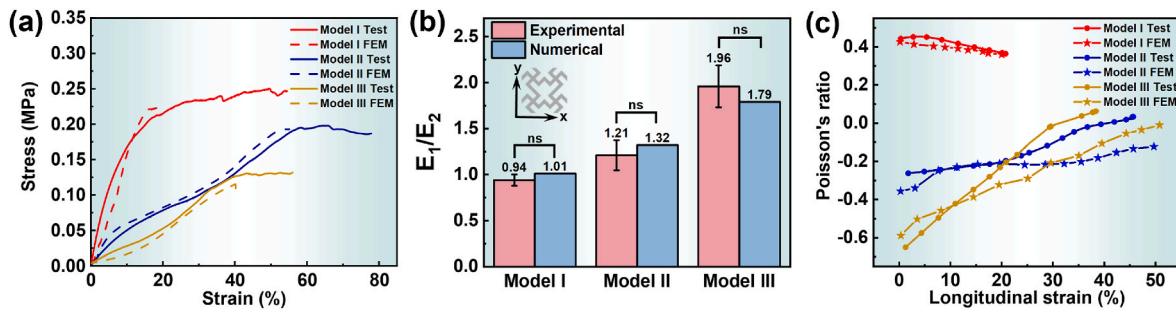

Fig. 5. Flow chart of finite element analysis.

Fig. 6. Comparative analysis of the test and numerical simulation results for three different cardiac patch types: (a) Strain-Stress Curves; (b) Modulus Ratio; (c) Poisson's Ratio.

Table 3
Comparative analysis for experimental results and simulated results.

Type	Data source	Yield strength (MPa)	Error	Poisson's ratio	Modulus ratio (E_1/E_2)	Error
Model I	Experiment	0.22	9.09 %	0.46	0.94	7.45 %
	Simulation	0.20		0.39	1.01	
Model II	Experiment	0.19	10.53 %	−0.26~0.03	1.21	9.09 %
	Simulation	0.17		−0.36~-0.12	1.32	
Model III	Experiment	0.13	7.69 %	−0.65~0.07	1.96	8.67 %
	Simulation	0.12		−0.59~-0.01	1.79	

rib features. Consequently, the strain energy retained under longitudinal tensile loading can be articulated as follows:

$$U_{ij} = \int \frac{(S_y s_i + F_x c_i)^2}{2EAc_i} dx_i + \int \frac{(S_y x_i + F_x y_i)^2}{2EIc_i} dx_i + \int \frac{(S_y s_j + F_x c_j)^2}{2EIc_j} dx_j$$
$$+ \int \frac{(S_y x_j + F_x y_j)^2}{2EIc_j} dx_j$$

(14)

Here, $S_i = \frac{dy_i}{dx_i} / \sqrt{1 + \left(\frac{dy_i}{dx_i}\right)^2}$, $c_i = 1 / \sqrt{1 + \left(\frac{dy_i}{dx_i}\right)^2}$.

Furthermore, E represents the elastic modulus of the PCL, $I = bt^3$ represents the rib section, $A = bt$ represents the cross-sectional area, b represents the width of the rib section, and t represents the thickness of the rib section.

Applying the second Kaplan's law, the deformations δ_x and δ_y of the unit cell along the x and y directions were determined as follows:

$$\delta_x = \frac{\partial U}{\partial F_x}\bigg|_{S_x=S_y=P_y=0}$$

(15)

$$\delta_y = \frac{\partial U}{\partial F_y}\bigg|_{S_x=S_y=P_x=0}$$

(16)

Furthermore, the equivalent stress and strain along the x and y directions were expressed as:

$$\varepsilon_x = \frac{\delta_x}{2L}$$
$$\varepsilon_y = \frac{\delta_y}{2L}$$

(17)

$$\sigma_x = \frac{F_x}{Lt}$$
$$\varepsilon_y = \frac{F_y}{Ft}$$

(18)

In conclusion, an auxetic structure exhibited both transverse and longitudinal expansion when subjected to stretching. This unique behavior was attributed to the chirality rotation of the unit cell during longitudinal stretching, coupled with outward expansion via its concave

sections. The synergy between chirality and concavity imparted auxetic properties to the structure, resulting in the auxetic effect. As observed in the deformation patterns shown in Fig. 7, when a tensile load was applied in the y direction, the deformation primarily stems from the transverse bending moment in the x direction, which predominated the structural deformation in all directions.

4. Results and discussion

4.1. The tensile property of cardiac patches

The unique deformation mechanism inherent to the auxetic structure endowed Models II and III with outstanding tensile properties. The differential stress-strain responses of these three types of patches were depicted in Fig. 8a–c. Model I, displaying classic elastic-plastic behavior, began to undergo irreversible plastic deformation when the strain reached 12%. In stark contrast, both types of auxetic patches demonstrated near-linear elastic stress-strain behavior over a much wider strain range, significantly exceeding 12%. The tensile test results for Model II indicated an almost linear trend within the 0–30 % strain range. Furthermore, the rate of stress increase became more gradual as the strain escalated. Once the strain of the patch surpassed 30%, the bent ribs within the structure were fully straightened, resulting in a sharp increase in stress until the plastic phase was reached. The yield strength of Model II was determined to be 0.19 MPa. Conversely, Model III exhibited a distinct trend with a less steep stress-strain curve. This difference was attributed to the arc structure having a shorter effective expansion path compared to the folded structure, leading to lower stiffness in Model III. Similarly, as the strain in Model III increased, the arc segment was completely straightened, leading to a greater increase in stress, mirroring the characteristics seen in Model II. The final yield strength of Model III was recorded at 0.13 MPa. Testing indicated that the designed auxetic patches II and III had yield limit strain of 55% and 38%, respectively, which were 4.5 and 3.1 times higher than that of the conventional Model I. This demonstrated their superior elasticity, making them more suitable as patches for large deformable biological tissues. Additionally, Models II and III possessed tensile modulus of 0.32 MPa and 0.31 MPa, respectively, aligning well with the modulus of natural human myocardium (0.15–0.4 MPa) [58,59]. Furthermore, these models exhibited high toughness, with Model II at 46.05 kJ/m^3
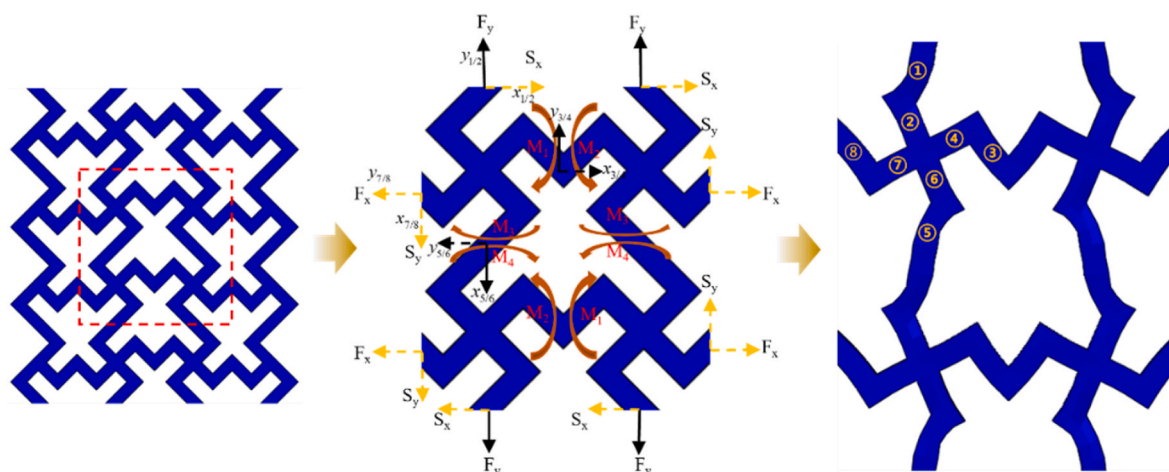
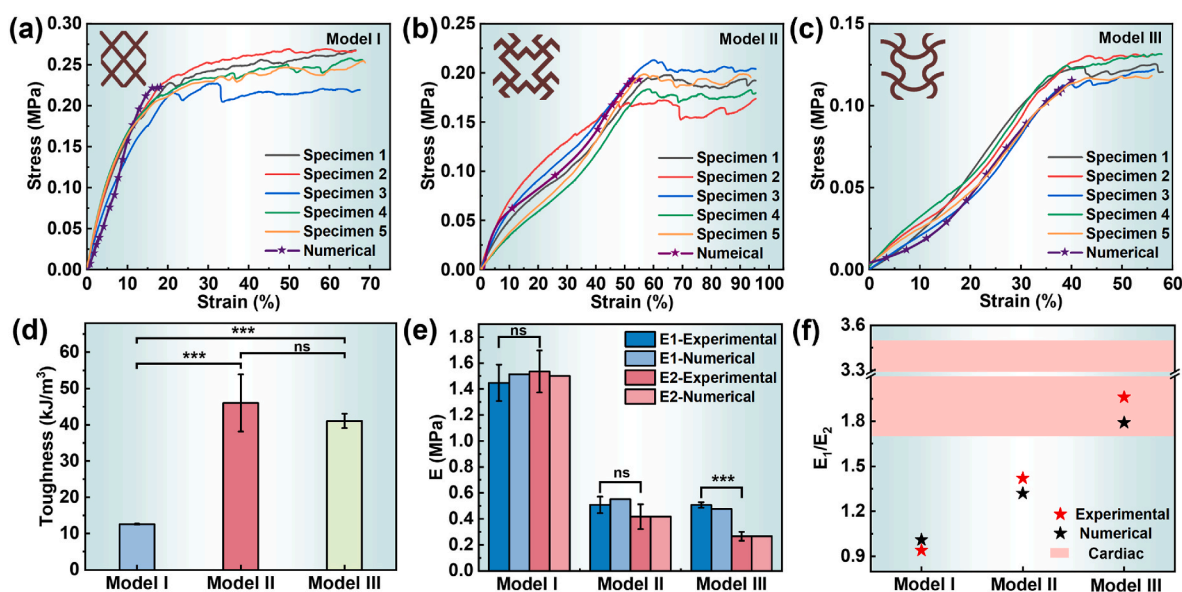**Fig. 7.** Schematic diagram of unit deformation under tensile load.

Fig. 8. Stress-strain curves of structures under tensile load: (a) Model I; (b) Model II; (c) Model III; (d) Toughness of three types of cardiac patches; (e) Transverse and longitudinal equivalent elastic modulus of the patches under tensile load; (f) Modulus ratio of the patches.

and Model III at 41.06 kJ/m³ (Fig. 8d), significantly surpassing Model I, with its toughness at 12.6 kJ/m³.

The biomechanical behavior of the heart reveals that during the heart's diastole phase, the modulus of transverse tissue (E_1) typically exceeds the modulus of longitudinal tissue (E_2), leading to anisotropic mechanical characteristics. The equivalent modulus ratio E_1/E_2 for cardiac tissue typically ranges between 1.70 and 3.50 [43]. To investigate the anisotropy of our designed patch and its efficacy in mechanical contraction under working conditions, we examined the equivalent modulus anisotropy ratios of different patch types. The results, as depicted in Fig. 8e, showed varied outcomes. Model I, with a diamond-shaped network structure in both transverse and longitudinal directions, exhibited almost identical modulus in both axes, resulting in an insignificant modulus ratio E_1/E_2 of 0.94, markedly lower than that of cardiac tissue. While Model II demonstrated some degree of the required anisotropy for cardiac repair, the contrast in modulus between the two directions remains relatively minor, with an equivalent modulus ratio of only 1.42, falling short of cardiac tissue requirements. In contrast, Model III exhibited significant anisotropy, with its equivalent modulus ratio reaching 1.96, aligning closely with the modulus ratio of

cardiac tissue. This indicated that the designed auxetic Model III mirrored the physiological tensile modulus of the human heart, possessing greater transverse stiffness than longitudinal stiffness, akin to natural heart tissue. Overall, the tensile mechanical behavior of Model III, as designed in this study, was more closely aligned with the inherent mechanical properties of cardiac biological tissue.

Simultaneously, failure process analysis of the patches under tensile load was also conducted using numerical simulations, as depicted in Fig. 9. The stress cloud diagram revealed that the stress in Model I was predominantly concentrated at the central intersection of the structure, especially at the nodal points, leading to early damage in the load-bearing center. As longitudinal strain increased, the structure of Model I contracted, leading to the reduction of porosity and causing the hydrogel to compress and bulge outwards. In the case of Model II, during stretching, the longitudinal bending ribs that bear the load were straightened, allowing the structure to expand and relax. Concurrently, the transverse bending ribs, formed by the rotation of its unit cells, also provided support, preventing pore shrinkage and inducing the auxetic effect within the structure. However, while the transverse ribs of Model II partially supported the longitudinal ribs and helped prevent pore
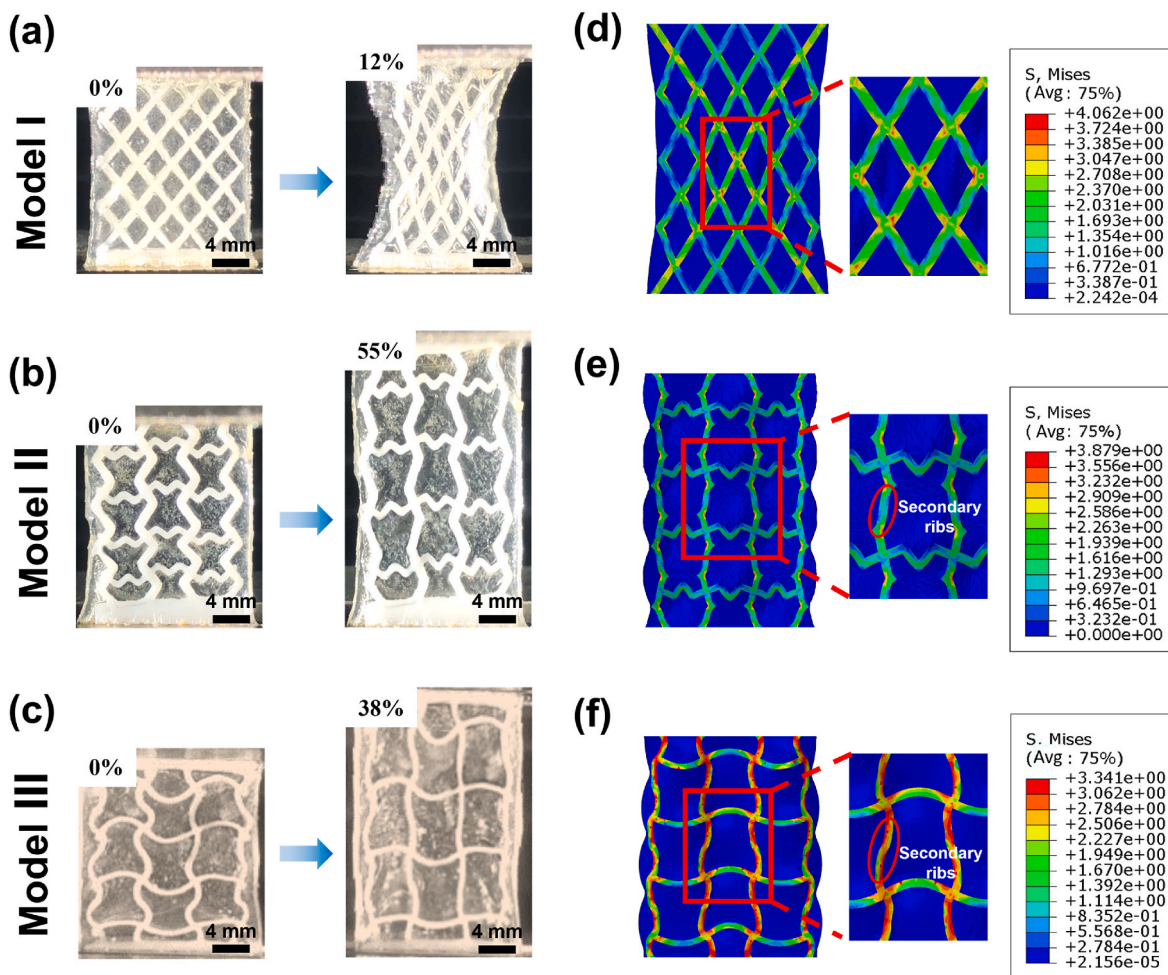
Fig. 9. (a–c) Experimental deformation test of Model I, Model II and Model III; (d–f) Finite element analysis of deformation of Model I, Model II and Model III.

contraction, they also led to significant bending of the secondary ribs, limiting their supportive capacity. In contrast, Model III utilized arc ribs in place of straight ribs, shortening the expansion path and avoiding folding and shrinkage, thereby creating a more effective expansion structure. Consequently, as the strain increased during stretching, Model III, with its arc segments, demonstrated an equivalent modulus ratio range more favorable for cardiac repair.

Fig. 10 illustrated the variation of the Poisson's ratio as a function of longitudinal strain up to the point of plastic deformation. The

displacement in the x-direction was defined as positive when moving left and negative when moving right, while displacement in the y-direction was considered positive when moving upward and negative when moving downward. Initially, the lateral displacement of the units on either side of the middle section was most pronounced, diminishing progressively towards the center, with symmetrical displacements on both the left and right sides. For Model I, when the longitudinal displacement reached approximately 2.56 mm, extreme contraction occurred and porosity significantly diminished [60]. Contrarily, Models
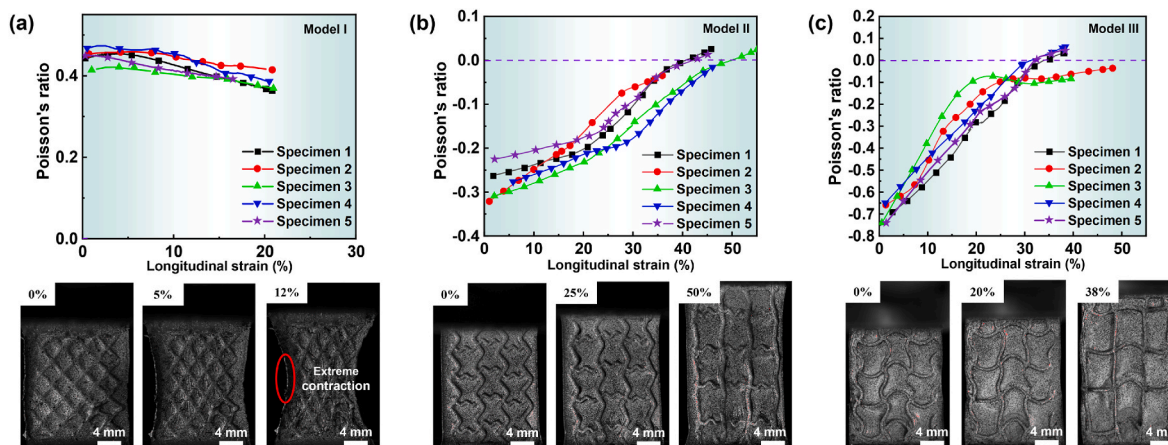

Fig. 10. The relationship of Poisson's ratio with longitudinal strain of (a) Model I; (b) Model II; (c) Model III.

II and III demonstrated the exact opposite trend. As the load increased, the absolute value of the structure's lateral displacement also increased, signifying a pronounced negative Poisson's ratio effect. The relationship between Poisson's ratio and longitudinal tensile strain was subsequently determined. The Poisson's ratio for the conventional patch, Model I, remained relatively constant at 0.46. In contrast, Models II and III exhibited a directional negative Poisson's ratio effect, with the Poisson's ratio increasing alongside longitudinal strain. The change of Poisson's ratio in Model II was segmented into three phases. Initially, it increased linearly with structural longitudinal strain. Then, at the 25% strain, the increase rate accelerated before entering the third phase where it slowed down again as the structure fully opened, reducing the auxetic performance. The entire process displayed an S-shaped variation in Poisson's ratio. The Poisson's ratio of Model III evolution differed slightly, mainly divided into two phases. In the first phase, it rose linearly at a rate significantly higher than Model II. As longitudinal strain outpaced transverse strain growth, the deformation ability weakened, leading to the stabilization of Poisson's ratio.

In conclusion, as the stretching process began, the ribs of the structure started to unfold and expand. This unfolding process allowed the structure to exhibit a high degree of auxetic behavior, reflected in the increasing slope of Poisson's ratio curve. However, upon reaching the yield strain, the structural ribs were essentially fully expanded. At this stage, the capacity for further mesh deformation is significantly reduced. Consequently, the ability of the structure to continue exhibiting auxetic properties diminished sharply. This reduction in deformation capacity led to a decrease in the slope of Poisson's ratio curve, until ultimately approaching a value close to zero, reaching the structural limitation of rib expansion and mesh deformation. This analysis demonstrated that the auxetic structures designed in this study exhibited excellent deformation and auxetic characteristics, aligning more closely with the physiological mechanical behavior of heart tissue. Additionally, the broader Poisson's ratio range of Model III significantly enhanced its potential applicability in future scenarios.

4.2. Damage analysis of auxetic scaffolds

All the conducted tests and simulations consistently demonstrated that under tensile load, the stress predominantly concentrates on the PCL auxetic scaffold, leading to significant damage to the ribs. Therefore, this section primarily addresses the damage failure analysis of the PCL auxetic scaffold to detect its specific load-bearing capacity. Utilizing the previously mentioned elastic-plastic constitutive model, the three types of scaffolds were directly simulated, and the damage evolution process was predicted using the flexible damage criterion, in conjunction with the experimental results. The tensile test and simulation outcomes for Scaffold I were presented in Fig. 11a and d. The test results indicated a significant decrease in the scaffold's porosity as the load increased, culminating in substantial structural contraction and a reduction of the grid area to 80% of its original size at the end of the loading period. This behavior contrasts sharply with the natural expansion property of the heart surface and does not align with the cardiac diastolic and contraction dynamics. Moreover, the simulation results revealed that at the 5% loading strain, the tensile stress was primarily concentrated on several central ribs, indicating an uneven stress distribution at this stage. As the scaffold was further stretched to the 12% strain, the stress concentration in the central rib became more pronounced, while the stress on the unit cells at either side of the structure was minimal, almost negating load bearing. At the end of loading, due to the force transmission along a fixed path, the load was predominantly borne by the main ribs in the center. Within a single unit cell, different ribs exhibited varied stress forms, and compression buckling occurred in certain sections. Thus, during the stretching process, for the conventional Scaffold I with the positive Poisson's ratio, damage initially manifested at the lower right corner connected to the fixed end and subsequently propagated upwards and downwards until failure.

For the auxetic Scaffold II, the tensile test and simulation results were displayed in Fig. 11b and e. During the initial loading phase, the stress within the scaffold was evenly distributed across the entire structure.
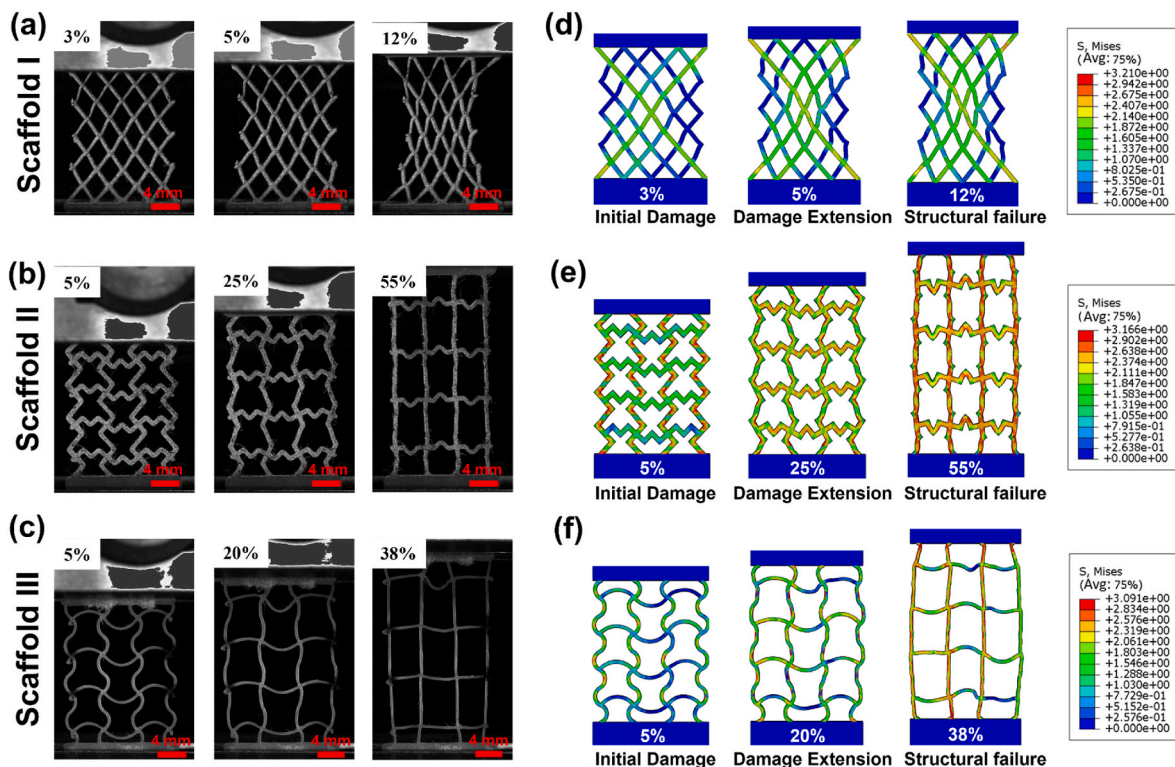

Fig. 11. Deformation mode of Scaffold I, Scaffold II and Scaffold III under: (a–c) tensile experiments; (d–f) finite element analysis.

This contrasted markedly with the uneven load distribution in Scaffold I, indicating that Scaffold II achieved more effective structural utilization. Furthermore, as the load incrementally increased, Scaffold II exhibited distinct structural characteristics compared to Scaffold I. First, regarding structural deformation, the structure of Scaffold II experienced lateral expansion while undergoing longitudinal stretching, leading to increased porosity. Consistent with the auxetic characteristics, the transverse ribs supported the longitudinal ribs in their rotational expansion, while concurrently undergoing compression and bending themselves. Secondly, concerning stress distribution, the stress across each unit cell of this structure was relatively uniform. However, local stress concentrations were also noted at the rib bends. Comparing the simulation outcomes of Scaffold I with Scaffold II, it is observed that at the 12% tensile strain, the maximum stress point of Model I reached 3.21 MPa, whereas, for Scaffold II, the maximum stress point was 3.17 MPa at a 50% strain. This suggested that the auxetic scaffolds endured lower stress points under higher strain and possessed superior load-bearing capabilities. At the end of the tensile loading, the test results showed a rib in the Scaffold II structure breaking from the middle, yet retaining some load-bearing capacity. Damage failure simulations of this process revealed that due to stress concentration, damage initially occurred at the rib bend, progressively expanded, and ultimately resulted in a break at the bend.

The tensile test results of the optimally designed auxetic Scaffold III, where folded ribs are replaced with arc ribs, were depicted in Fig. 11c and f. From the onset of loading up to the 38% strain, there was a notable reduction in stress concentration, and the stress was more evenly distributed throughout the structure. Meanwhile, Scaffold II shared similar deformation characteristics with Scaffold II, expanding laterally during longitudinal stretching. However, the transverse ribs in Scaffold III, unlike those in Scaffold II, provided greater space for expansion due to their arc-shaped design. Consequently, Scaffold III exhibited a more extensive range of auxetic effect compared to Scaffold II. Furthermore, the damage simulation results revealed that, upon full stretching of the structure, the initiation of damage occurred randomly, with the final breakage emanating from the loading end, which was also confirmed by many other research illustrating that the 'localized contraction' phenomenon typically occurs near fixtures or points of stress concentration [61–63].

4.3. The fatigue resistance of composite patches

The cyclic loading-unloading tensile test results clearly demonstrated the excellent fatigue resistance of the auxetic patches designed in this study. Fig. 12 illustrated the cyclic strain-stress curves for representative specimens from each model at 22% and 30% strain levels, respectively. Notably, there is a marked difference between the first cycle curve and subsequent cycles. As the number of cycles increased, this difference diminished and stabilized after approximately 300 cycles. During the 0–22% strain cycle, as shown in Fig. 12a-c, the maximum stress for Model I reduced from 0.242 MPa to 0.180 MPa, indicating a 25.62% decrease. The maximum stress for Model II decreased by 17.9 %, from 0.078 MPa to 0.064 MPa. Model III exhibited the least reduction in maximum stress, decreasing from 0.059 MPa to 0.051 MPa, a reduction of 13.56%. This indicated that Model I experienced the greatest stress drop, possibly due to exceeding its elastic stress limit under the 22% strain cycle, resulting in unrecoverable plastic deformation and thus more strain energy loss compared to the other models. Models II and III initially showed noticeable hysteresis curves due to polymer stress softening, but these curves gradually stabilized with increasing cycle numbers. Moreover, Model III, with the smallest decrease in maximum stress, demonstrated superior recoverable elastic deformation. This suggests that Model III possessed the best auxetic expansion and contraction capabilities within its strain range, offering significant application potential in scenarios involving continuous heartbeats.

In the cyclic loading test under 30% strain control, the stress-strain curve exhibited a similar pattern to that observed in the 22% strain cycle. Effective strain energy dissipation predominantly occurred during the first cycle, and as the number of cycles increased, the curves exhibited a progressively overlapping trend, as illustrated in Fig. 12d-f. Notably, under the 30% strain cycle, Model I displayed a significantly larger first-cycle hysteresis loop compared to the lower strain cycle, indicating substantial plastic deformation at this level of cyclic strain. However, Models II and III continued to demonstrate the same impressive recovery ability as observed under the 22% strain cycle. Therefore, under the 30% strain cyclic regime, Model I was likely to undergo extensive damage, leading to irrecoverable deformation, whereas Models II and III could essentially revert to their original shapes, with subsequent hysteresis curves nearly overlapping, suggesting that the structures with auxeticity remain relatively intact throughout the cycle.

These experimental observations indicated that effective strain
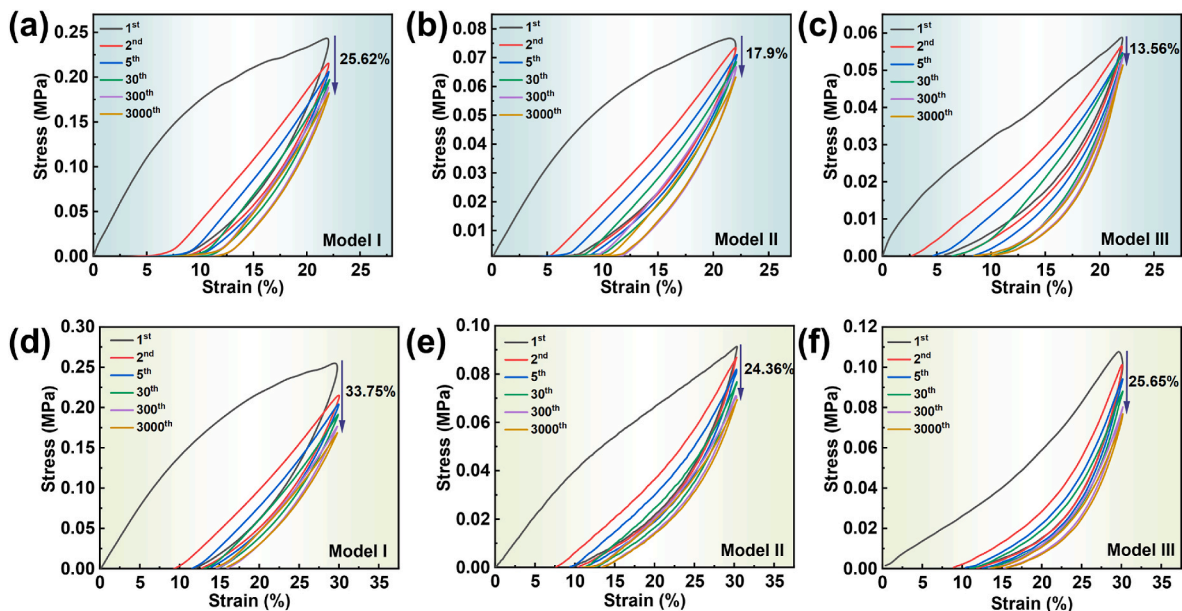

Fig. 12. Stress-strain curves of Model I, Model II, and Model III at: (a–c) 22 % cyclic strain; (d–f) 30 % cyclic strain.

energy dissipation for all patch types primarily occurred in the first cycle. With increasing cycle numbers, stress softening ensued, resulting in non-overlapping stress-strain curves. Additionally, as the fatigue cycle duration extended, local molecular segments of the patches rearranged, relaxing the interactions among tightly cross-linked polymer chains to a lower energy state, thereby reducing modulus. Part of the lost strain energy also gradually lowered the maximum stress the patch can endure. After a certain number of cycles, however, the internal structure interactions reached an equilibrium due to elasticity, leading to an almost complete overlap between the 300th and 3000th cycle curves for Model II and III. It is important to note that after multiple cycles, the zero-stress point in the figures gradually shifted away from the origin, indicative of the compressive buckling and negative stress generation in the composite hydrogel due to residual tensile stress in each cycle.

4.4. Influence of different design parameters on the mechanical properties of composite patches

4.4.1. Effect of node rib deflection angle

To investigate the influence of varying node rib deflection angles on the modulus ratio, Poisson's ratio, and other mechanical properties of patches, structural finite element simulations were conducted for patches with different deflection angles, as depicted in Fig. 13a–c. While maintaining other parameters consistent with the initial design, the impact of the node rib deflection angle β on the mechanical properties of the structures was examined. Fig. 13a illustrated the deformation units of auxetic patches with deflection angles of 15°, 45°, and 75°. As presented in Fig. 13b, during the transition of the deflection angle from β = 15° to β = 75°, the modulus ratio of the auxetic patches changed smoothly. Specifically, the modulus ratio of Model II decreased from 2.27 to 0.75, a 70% reduction, while the modulus ratio of Model III dropped from 3.95 to 1.32, a 66% decrease. Adjusting the node rib deflection angle enabled the designed auxetic patch to achieve an equivalent modulus ratio comparable to that of natural heart tissue. It is observed that at smaller deflection angles (β < 30°), Model II and III exhibited larger equivalent modulus ratios, aligning more closely with cardiac tissue. This could be attributed to the auxetic structure of the patches, a combination of chiral rotation and concave angle structures. That is, with smaller deflection angles, the longitudinal ribs bend more

during longitudinal stretching, allowing greater expansion compared to the transverse ribs. Consequently, during transverse stretching, the transverse ribs, due to lesser bending and strain, have a larger modulus in the transverse direction than in the longitudinal direction. As the deflection angle increases, the modulus ratio gradually decreases due to different load transfers in longitudinal versus transverse stretching. Larger deflection angles lead to increased bending of the transverse ribs, allowing more expansion space and thus increasing transverse strain under transverse loading while reducing longitudinal strain under longitudinal loading. This results in a decrease in transverse modulus E_1 and an increase in longitudinal modulus E_2, lowering the modulus ratio with increasing deflection angle. Notably, at any deflection angle, the modulus ratio of Model III was higher than that of Model II. This was because Model III, composed of an arc structure without redundant bending ribs and a shorter force transmission path, consistently maintained a higher modulus ratio than Model II, making Model III aligned more suitably with the anisotropic concept for cardiac patches.

In addition, the trend of Poisson's ratio variation for Model II and Model III under different deflection angles was also examined, with results presented in Fig. 13c. As the deflection angle increases from 15° to 45°, the absolute value of the overall Poisson's ratio of the structure gradually ascended. This ascent continued until the deflection angle reached 45°, at which point the node ribs of both patch types became orthogonal, leading to the maximum absolute value of Poisson's ratio. During this process, the rate of change in the Poisson's ratio progressively slowed down. This is likely because as the angle between the transverse and longitudinal ribs and the horizontal line increased, the component force exerted on the transverse ribs during the rotation of the chiral unit cell decreased. Consequently, the rate of strain change relative to the longitudinal ribs also diminished, leading to a deceleration in the slope of Poisson's ratio change until it approached zero. Furthermore, while Model III also exhibited its largest absolute Poisson's ratio value at a 45° node deflection angle, it demonstrated a broader range of Poisson's ratio variation by optimizing the bent rib into an arc rib. In terms of the trend with node deflection angle, the arc rib, having a more efficient force transmission path compared to the bent rib, maintained a consistent rising trend in Poisson's ratio with longitudinal strain across different deflection angles, ranging from 15° to 75°. There is no yielding or bending phenomenon in the transverse rib of Model III as seen in
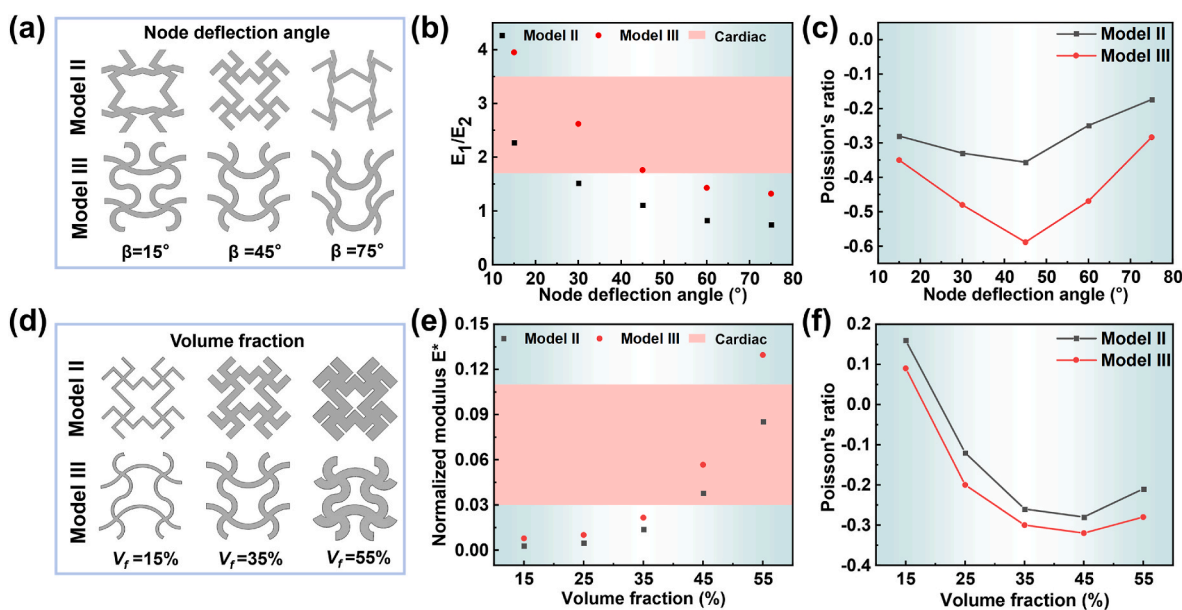

Fig. 13. (a) Deformation units with node deflection angles of 15°, 45° and 75°; (b) Structural modulus ratio changes with node deflection angle; (c) Structural Poisson's ratio changes with node deflection angle; (d) Deformation units with volume fractions of 15 %, 35 % and 55 %; (e) Structural normalized modulus changes with volume fraction; (f) Structural Poisson's ratio changes with volume fraction.

Model II, resulting in a similar Poisson's ratio increase across various deflection angles. Additionally, in terms of Poisson's ratio range variation with node deflection angle, the presence of the arc structure allowed Model III to exhibit a wider range of Poisson's ratio values. Its minimum Poisson's ratio approached −0.6, double that of Model II. This capability enabled Model III to control the Poisson's ratio more precisely, allowing cardiac patches designed with this structure to offer greater adaptability, potentially meeting the needs of patients across different ages or health conditions.

4.4.2. *Effect of volume fractions*

Simultaneously, for Model II and III, auxetic structures with varying volume fractions (V_f) were designed, as shown in Fig. 13d. As the volume fraction increased, the structural ribs widened, enhancing both the transverse and longitudinal modulus and stiffness of the structure. Consequently, the normalized modulus of both Model II and III was significantly improved. Notably, when the volume fraction of the patch approached 55%, the degree of chiral rotation and concave angle rotation diminished, leading to limited structural expansion, resulting in a sharp increase in the normalized modulus E* modulus. This characteristic provided the designed patch with additional control over its mechanical properties. Besides needing an equivalent modulus ratio that aligns with cardiac tissue, controlling the volume fraction enabled an auxetic scaffold to achieve a normalized modulus matching that of cardiac tissue. It is evident from the figure that at higher volume fractions ($45\% \leq V_f \leq 55\%$), the normalized modulus of Medel II and Model III closely matched that of the heart, enhancing their suitability as cardiac repairing patches. Moreover, at any given volume fraction, the normalized modulus of Model III was higher than that of Model II, making it a more favorable candidate for future cardiac patches.

In addition, the Poisson's ratio of the structure under a 10% strain was chosen as the focal point to examine the impact of volume fraction on the Poisson ratio trend. As depicted in Fig. 13f, the Poisson's ratio initially decreased and then increased with the rise in structure volume fraction. This phenomenon may be attributed to the fact that at a 15% volume fraction, the structural ribs were narrow, possessing a lower load-bearing capacity. Consequently, the transverse ribs of the structure were not fully able to provide support for lateral expansion, leading to a quasi-staggered network structure in Model II and III, thus inducing a positive Poisson's ratio effect. However, as the volume fraction increased, the rib width incrementally expanded, enhancing the rotational support function inherent in the auxetic structure, and thereby progressively intensifying the structure's auxetic effect. The absolute value of the Poisson's ratio peaked at a 45% volume fraction. Yet, with a further increase in the volume fraction, both the transverse and longitudinal ribs broadened, diminishing the rotational effect of the chiral and concave-angle units, and consequently reducing the auxetic capacity of the structure. At this juncture, the absolute value of Poisson's ratio of the structure started to decline, as indicated by the upward trend of the curve.

5. Conclusion

In this study, Model II and optimized Model III exhibiting the auxetic effect were designed through the combination of chiral rotation and concave-angle units. Additionally, two-phase composite patches suitable for myocardial damage repair were successfully developed by integrating the scaffolds prepared by 3D printing with the biocompatible hydrogel. The mechanical properties of both the positive Poisson's ratio and auxetic patches were comparatively analyzed through tensile and cyclic loading tests. The findings revealed that the elastic limit strain of Model II and Model III were 4.5 times and 3.1 times greater than that of Model I, respectively. Moreover, both of the auxetic patches demonstrated excellent elasticity and recovery capabilities within the physiological strain range of cardiac tissue. Notably, Model III aligned more

closely with cardiac tissue in terms of modulus parameters and Poisson's ratio range, and its toughness reached 41.06 kJ/m³. When meeting strength requirements, it exhibited a mechanical behavior pattern more akin to that of cardiac tissue. Under cyclic loading conditions, Model III also displayed superior performance. Numerical simulations further indicated that Model III had enhanced tensile properties, with its unique arc ribs significantly reducing the stress concentration of the overall structure. Moreover, Model III, based on its former Model II design, was more responsive to design parameters, facilitating the achievement of adjustable modulus and Poisson's ratio to fulfill the customized requirements. Consequently, the auxetic cardiac patches of this study could contribute to the advancement of biomimetic designs for patches used in heart tissue engineering.

CRediT authorship contribution statement

Zhicheng Dong: Writing – original draft, Methodology, Conceptualization. **Xiaoyang Ren:** Writing – review & editing, Software. **Ben Jia:** Writing – review & editing, Investigation, Funding acquisition. **Xuanjia Zhang:** Validation, Data curation, Conceptualization. **Xiaopeng Wan:** Project administration. **Yang Wu:** Investigation, Data curation. **Heyuan Huang:** Supervision, Project administration, Funding acquisition.

Declaration of competing interest

The authors declare that they have no known competing financial interests or personal relationships that could have appeared to influence the work reported in this paper.

Data availability

Data will be made available on request.

References

[1] A. D'Amore, T. Yoshizumi, S.K. Luketich, M.T. Wolf, X. Gu, M. Cammarata, et al., Bi-layered polyurethane – extracellular matrix cardiac patch improves ischemic ventricular wall remodeling in a rat model, Biomaterials 107 (2016) 1–14.
[2] B. Lindahl, N.L. Mills, A new clinical classification of acute myocardial infarction, Nat. Med. 29 (2023) 2200–2205.
[3] C. Kuppe, R.O. Ramirez Flores, Z. Li, S. Hayat, R.T. Levinson, X. Liao, et al., Spatial multi-omic map of human myocardial infarction, Nature 608 (2022) 766–777.
[4] J. Liu, J. Wang, Y-f Xue, T-t Chen, D-n Huang, Y-x Wang, et al., Biodegradable phosphorylcholine copolymer for cardiovascular stent coating, J. Mater. Chem. B 8 (2020) 5361–5368.
[5] Y. Wang, G. Chen, H. Zhang, C. Zhao, L. Sun, Y. Zhao, Emerging functional biomaterials as medical patches, ACS Nano 15 (2021) 5977–6007.
[6] U. Tariq, M. Gupta, S. Pathak, R. Patil, A. Dohare, S.K. Misra, Role of biomaterials in cardiac repair and regeneration: therapeutic intervention for myocardial infarction, ACS Biomater. Sci. Eng. 8 (2022) 3271–3298.
[7] G. Theocharidis, H. Yuk, H. Roh, L. Wang, I. Mezghani, J. Wu, et al., A strain-programmed patch for the healing of diabetic wounds, Nat. Biomed. Eng. 6 (2022) 1118–1133.
[8] Q. Liu, S. Tian, C. Zhao, X. Chen, I. Lei, Z. Wang, et al., Porous nanofibrous poly(l-lactic acid) scaffolds supporting cardiovascular progenitor cells for cardiac tissue engineering, Acta Biomater. 26 (2015) 105–114.

[9] A. Gelmi, A. Cieslar-Pobuda, E. de Muinck, M. Los, M. Rafat, E.W.H. Jager, Direct mechanical stimulation of stem cells: a beating electromechanically active scaffold for cardiac tissue engineering, Adv. Healthcare Mater. 5 (2016) 1471–1480.

[10] E. Cao, Z. Dong, X. Zhang, Z. Zhao, X. Zhao, H. Huang, Mechanical properties and failure analysis of 3D-printing micron-scale ceramic-based triply periodic minimal surface scaffolds under quasi-static-compression and low-speed impact loads, Compos. Sci. Technol. 243 (2023) 110248.

[11] A. Zielińska, J. Karczewski, P. Eder, T. Kolanowski, M. Szalata, K. Wielgus, et al., Scaffolds for drug delivery and tissue engineering: the role of genetics, J. Contr. Release 359 (2023) 207–223.

[12] V. Hernandez, R.S. Jordan, I.M. Hill, B. Xu, C. Zhai, D. Wu, et al., Deformation rate-adaptive conducting polymers and composites, Small 19 (2023) 2207100.

[13] H. Haag, P.D. Dalton, V. Bloemen, The synergy of biomimetic design strategies for tissue constructs, Adv. Funct. Mater. 32 (2022) 2201414.

[14] Z. Li, W. Gao, M. Yu Wang, C.H. Wang, Z. Luo, Three-dimensional metamaterials exhibiting extreme isotropy and negative Poisson's ratio, Int. J. Mech. Sci. 259 (2023) 108617.

[15] K. Huang, E.W. Ozpinar, T. Su, J. Tang, D. Shen, L. Qiao, et al., An off-the-shelf artificial cardiac patch improves cardiac repair after myocardial infarction in rats and pigs, Sci. Transl. Med. 12 (2020) eaat9683.

[16] K.D. Dwyer, K.L.K. Coulombe, Cardiac mechanostructure: using mechanics and anisotropy as inspiration for developing epicardial therapies in treating myocardial infarction, Bioact. Mater. 6 (2021) 2198–2220.

[17] N. Munding, M. Fladung, Y. Chen, M. Hippler, A.D. Ho, M. Wegener, et al., Bio-metamaterials for mechano-regulation of mesenchymal stem cells, Adv. Funct. Mater. (2023) 2301133 n/a.

[18] Cui H, Liu C, Esworthy T, Huang Y, Yu Z-x, Zhou X, et al. 4D physiologically adaptable cardiac patch: a 4-month in vivo study for the treatment of myocardial infarction. Sci. Adv..6:eabb5067..

[19] Tang J, Wang J, Huang K, Ye Y, Su T, Qiao L, et al. Cardiac cell–integrated microneedle patch for treating myocardial infarction. Sci. Adv..4:eaat9365..

[20] C. Huang, L. Chen, Negative Poisson's ratio in modern functional materials, Adv. Mater. 28 (2016) 8079–8096.

[21] X.-T. Wang, B. Wang, Z.-H. Wen, L. Ma, Fabrication and mechanical properties of CFRP composite three-dimensional double-arrow-head auxetic structures, Compos. Sci. Technol. 164 (2018) 92–102.

[22] M. Kapnisi, C. Mansfield, C. Marijon, A.G. Guex, F. Perbellini, I. Bardi, et al., Auxetic cardiac patches with tunable mechanical and conductive properties toward treating myocardial infarction, Adv. Funct. Mater. 28 (2018) 1800618.

[23] H.M.A. Kolken, A.F. Garcia, A. Du Plessis, C. Rans, M.J. Mirzaali, A.A. Zadpoor, Fatigue performance of auxetic meta-biomaterials, Acta Biomater. 126 (2021) 511–523.

[24] W. Zhang, P. Soman, K. Meggs, X. Qu, S. Chen, Tuning the Poisson's ratio of biomaterials for investigating cellular response, Adv. Funct. Mater. 23 (2013) 3226–3232.

[25] Y. Yan, Y. Li, L. Song, C. Zeng, Y. Li, Pluripotent stem cell expansion and neural differentiation in 3-D scaffolds of tunable Poisson's ratio, Acta Biomater. 49 (2017) 192–203.

[26] X. Chen, C. Liu, M. Wadsworth, E.Z. Zeng, T. Driscoll, C. Zeng, et al., Surface engineering of auxetic scaffolds for neural and vascular differentiation from human pluripotent stem cells, Adv. Healthcare Mater. 12 (2023) 2202511.

[27] C. Wang, Y. Chai, X. Wen, Y. Ai, H. Zhao, W. Hu, et al., Stretchable and anisotropic conductive composite hydrogel as therapeutic cardiac patches, ACS Mater. Lett. 3 (2021) 1238–1248.

[28] N. Zanjanizadeh Ezazi, R. Ajdary, A. Correia, E. Mäkilä, J. Salonen, M. Kemell, et al., Fabrication and characterization of drug-loaded conductive poly(glycerol sebacate)/nanoparticle-based composite patch for myocardial infarction applications, ACS Appl. Mater. Interfaces 12 (2020) 6899–6909.

[29] M.M. Sayed, H.M. Mousa, M.R. El-Aassar, N.M. El-Deeb, N.M. Ghazaly, M. M. Dewidar, et al., Enhancing mechanical and biodegradation properties of polyvinyl alcohol/silk fibroin nanofibers composite patches for Cardiac Tissue Engineering, Mater. Lett. 255 (2019) 126510.

[30] H. Huang, Z. Dong, X. Ren, B. Jia, G. Li, S. Zhou, et al., High-strength hydrogels: fabrication, reinforcement mechanisms, and applications, Nano Res. 16 (2023) 3475–3515.

[31] B. Jia, H. Huang, Z. Dong, X. Ren, Y. Lu, W. Wang, et al., Degradable biomedical elastomers: paving the future of tissue repair and regenerative medicine, Chem. Soc. Rev. 53 (2024) 4086–4153.

[32] D. Olvera, M. Sohrabi Molina, G. Hendy, M.G. Monaghan, Electroconductive melt electrowritten patches matching the mechanical anisotropy of human myocardium, Adv. Funct. Mater. 30 (2020) 1909880.

[33] C. Wu, B. Wan, A. Entezari, J. Fang, Y. Xu, Q. Li, Machine learning-based design for additive manufacturing in biomedical engineering, Int. J. Mech. Sci. 266 (2024) 108828.

[34] P. Soman, J.W. Lee, A. Phadke, S. Varghese, S. Chen, Spatial tuning of negative and positive Poisson's ratio in a multi-layer scaffold, Acta Biomater. 8 (2012) 2587–2594.

[35] Z. Wang, C. Luan, G. Liao, J. Liu, X. Yao, J. Fu, Progress in auxetic mechanical metamaterials: structures, characteristics, manufacturing methods, and applications, Adv. Eng. Mater. 22 (2020) 2000312.

[36] P. Chansoria, E.L. Etter, J. Nguyen, Regenerating dynamic organs using biomimetic patches, Trends Biotechnol. 40 (2022) 338–353.

[37] X.-T. Wang, B. Wang, X.-W. Li, L. Ma, Mechanical properties of 3D re-entrant auxetic cellular structures, Int. J. Mech. Sci. 131–132 (2017) 396–407.

[38] M. Montgomery, S. Ahadian, L. Davenport Huyer, M. Lo Rito, R.A. Civitarese, R. D. Vanderlaan, et al., Flexible shape-memory scaffold for minimally invasive delivery of functional tissues, Nat. Mater. 16 (2017) 1038–1046.

[39] J.W. Lee, P. Soman, J.H. Park, S. Chen, D.-W. Cho, A tubular biomaterial construct exhibiting a negative Poisson's ratio, PLoS One 11 (2016) e0155681.

[40] E. Askari, I.F. Cengiz, J.L. Alves, B. Henriques, P. Flores, M.C. Fredel, et al., Micro-CT based finite element modelling and experimental characterization of the compressive mechanical properties of 3-D zirconia scaffolds for bone tissue engineering, J. Mech. Behav. Biomed. Mater. 102 (2020) 103516.

[41] I. Cockerill, C.W. See, M.L. Young, Y. Wang, D. Zhu, Designing better cardiovascular stent materials: a learning curve, Adv. Funct. Mater. 31 (2021) 2005361.

[42] H. Huang, X. Zhang, Z. Dong, X. Zhao, B. Guo, Nanocomposite conductive tough hydrogel based on metal coordination reinforced covalent Pluronic F-127 micelle network for human motion sensing, J. Colloid Interface Sci. 625 (2022) 817–830.

[43] P. Chansoria, J. Blackwell, E.L. Etter, E.E. Bonacquisti, N. Jasiewicz, T. Neal, et al., Rationally designed anisotropic and auxetic hydrogel patches for adaptation to dynamic organs, Adv. Funct. Mater. 32 (2022) 2207590.

[44] J.H. Park, H.-J. Park, S.J. Tucker, S.K. Rutledge, L. Wang, M.E. Davis, et al., 3D printing of poly-ε-caprolactone (PCL) auxetic implants with advanced performance for large volume soft tissue engineering, Adv. Funct. Mater. 33 (2023) 2215220.

[45] D. Liu, W. Nie, D. Li, W. Wang, L. Zheng, J. Zhang, et al., 3D printed PCL/SrHA scaffold for enhanced bone regeneration, Chem. Eng. J. 362 (2019) 269–279.

[46] V. Trakoolwannachai, P. Kheolamai, S. Ummartyotin, Characterization of hydroxyapatite from eggshell waste and polycaprolactone (PCL) composite for scaffold material, Compos. B Eng. 173 (2019) 106974.

[47] P.K. Penumakala, J. Santo, A. Thomas, A critical review on the fused deposition modeling of thermoplastic polymer composites, Compos. B Eng. 201 (2020) 108336.

[48] O.A. Mohamed, S.H. Masood, J.L. Bhowmik, Optimization of fused deposition modeling process parameters: a review of current research and future prospects, Advances in Manufacturing. 3 (2015) 42–53.

[49] J. Gu, Z. Lv, Y. Wu, Y. Guo, L. Tian, H. Qiu, et al., Dielectric thermally conductive boron nitride/polyimide composites with outstanding thermal stabilities via in-situ polymerization-electrospinning-hot press method, Compos. Appl. Sci. Manuf. 94 (2017) 209–216.

[50] A. Miller, C. Brown, G. Warner, Guidance on the Use of Existing ASTM Polymer Testing Standards for ABS Parts Fabricated Using FFF, vol. 3, 2019.

[51] Li X, Cui K, Zheng Y, Ye YN, Yu C, Yang W, et al. Role of hierarchy structure on the mechanical adaptation of self-healing hydrogels under cyclic stretching. Sci. Adv..9:eadj6856..

[52] O. Holzmond, X. Li, In situ real time defect detection of 3D printed parts, Addit. Manuf. 17 (2017) 135–142.

[53] B. Ling, K. Wei, Z. Wang, X. Yang, Z. Qu, D. Fang, Experimentally program large magnitude of Poisson's ratio in additively manufactured mechanical metamaterials, Int. J. Mech. Sci. 173 (2020) 105466.

[54] W. Liu, Y. Zhang, Z. Guo, D. Li, S. Zhao, W. Xie, Analyzing in-plane mechanics of a novel honeycomb structure with zero Poisson's ratio, Thin-Walled Struct. 192 (2023) 111134.

[55] M. Sadegh Ebrahimi, M. Noruzi, R. Hamzehei, E. Etemadi, R. Hashemi, Revolutionary auxetic intravascular medical stents for angioplasty applications, Mater. Des. 235 (2023) 112393.

[56] X. Zhao, B.L. Guo, H. Wu, Y.P. Liang, P.X. Ma, Injectable antibacterial conductive nanocomposite cryogels with rapid shape recovery for noncompressible hemorrhage and wound healing, Nat. Commun. 9 (2018) 1–17.

[57] J.-P. Brincat, K.M. Azzopardi, A. Buttigieg, F. Scarpa, J.N. Grima, R. Gatt, Foams as 3D perforated systems: an analysis of their Poisson's ratios under compression, Phys. Status Solidi 251 (2014) 2233–2238.

[58] X. Song, X. Wang, J. Zhang, S. Shen, W. Yin, G. Ye, et al., A tunable self-healing ionic hydrogel with microscopic homogeneous conductivity as a cardiac patch for myocardial infarction repair, Biomaterials 273 (2021) 120811.

[59] L.-M. Zhao, L. Wang, W.-Q. Zhang, R. Wang, X.-Z. Zhang, X.-X. Lei, et al., Promotion of right ventricular outflow tract reconstruction using a novel cardiac patch incorporated with hypoxia-pretreated urine-derived stem cells, Bioact. Mater. 14 (2022) 206–218.

[60] D.Y. Fozdar, P. Soman, J.W. Lee, L.-H. Han, S. Chen, Three-dimensional polymer constructs exhibiting a tunable negative Poisson's ratio, Adv. Funct. Mater. 21 (2011) 2712–2720.

[61] Y. Zhu, D. Gao, Y. Shao, H. Chen, C. Yu, Q. Wang, A novel prefabricated auxetic honeycomb meta-structure based on mortise and tenon principle, Compos. Struct. 329 (2024) 117782.

[62] W. Zhang, H. Wang, X. Lou, Z. Yan, J. Shao, T. Wu, et al., On in-plane crushing behavior of a combined re-entrant double-arrow honeycomb, Thin-Walled Struct. 194 (2024) 111303.

[63] C. Zhang, F. Lu, T. Wei, X. Ling, B. Lin, Y. Zhu, On the collapse stress of tubular enhanced anti-tetra-missing rib structure, Thin-Walled Struct. 199 (2024) 111801.